Linear analysis of cross-field dynamics with feedback instability on detached divertor plasmas

Linear analysis of cross-field dynamics with feedback instability on detached divertor plasmas

Hiroki Hasegawa[1,2], **Hirohiko Tanaka**[3] **and Seiji Ishiguro**[1,2]

[1] National Institute for Fusion Science (NIFS), National Institutes of Natural Sciences (NINS), Toki, Gifu, Japan

[2] Department of Fusion Science, The Graduate University for Advanced Studies, SOKENDAI, Toki, Gifu, Japan

[3] Graduate School of Engineering, Nagoya University, Nagoya, Aichi, Japan

E-mail: `hasegawa.hiroki@nifs.ac.jp`

May 2021

Abstract. The theoretical model of the feedback instability is proposed to explain the mechanism of the correlation between the detachment and the cross-field plasma transport. It is shown that the feedback instability on the detached divertor plasma can be induced in a certain condition in which the volume recombination frequency is larger than the ion cyclotron frequency in the recombination region. Further, the density gradient and the electric field in the direction perpendicular to the magnetic flux surface are not zero in the condition. The feedback instability can provide the cross-field plasma transport in the boundary layer of magnetic fusion torus devices. Furthermore, the properties of the radial transport observed in the NAGDIS-II linear device experiment are compared with the estimation by the feedback instability model. The dependence of the feedback instability mode on the total collision frequency and the recombination coefficient and the density gradient has been also investigated. Although the dependency on the total collision frequency and the recombination coefficient for the typical fusion torus device case is opposite to that for the NAGDIS-II case, the represented dependencies show the reasonable tendency in each case.

PACS numbers: 52.25.Xz, 52.35.-g, 52.40.Hf, 52.55.Rk, 52.25.Fi

Keywords: detached divertor plasma, cross-field transport, feedback instability
Submitted to: *Nucl. Fusion*

1. Introduction

The correlation between the detachment [1] and the non-diffusive cross-field plasma transport in the boundary layer has been reported in various magnetic confinement devices. These are tokamak [2, 3], helical [4] and linear [5, 6, 7, 8, 9, 10, 11, 12] devices. Such a correlation is expected to expand the width of the heat flux to the

divertor target, i.e., λ_{q}. Thus, the observation and analysis regarding the correlation phenomena have been actively performed in linear devices, e.g., the NAGDIS-II [5, 6, 7, 8, 13, 14, 15, 16, 17, 18, 19, 20]. However, the physical dynamics of the correlation has not been revealed sufficiently. On the other hand, the detached divertor plasma can be considered as the coupling of two magnetized plasmas characterized by different current mechanisms. Such a coupling system is also found in the space plasma as the magnetosphere-ionosphere (M-I) coupling. The electric current in the magnetosphere streams along the geomagnetic field line, while that in the ionosphere can flow in the direction perpendicular to the geomagnetic field because the frequency of collision between ions and neutrals ν_{in} is larger than the ion cyclotron frequency Ω_{ci} [21]. This difference of the current mechanism between the magnetosphere and the ionosphere can induce the instability called "feedback instability" [22]. The field-aligned current (FAC) and the ionosphere plasma density grow locally by the feedback instability and auroral arcs are formed in the region where FAC is enhanced [23, 24, 25].

In this study, we investigate the cross-field dynamics in the detached plasma state with the coupling model between magnetized plasmas characterized by different current mechanisms as described above. In the recombination region in front of a divertor target, the volume recombination frequency ν_{rec} can be larger than Ω_{ci} because of the high density and the low temperature. In such a situation, the cross-field motion of ions is mainly in the direction of the electric field, while that of electrons is almost in the direction of the $\boldsymbol{E} \times \boldsymbol{B}$ drift. Thus, the difference in the direction of motion may provide the cross-field current in the recombination region. On the other hand, the cross-field current can be generated by only the polarization and the diamagnetic drifts in the upstream plasma. We have considered whether such a difference between the current mechanisms in each region induces the cross-field plasma transport. In Sec. 2, the linear dispersion relation is derived on the basis of the coupling model. In Sec. 3, it is shown that one mode of the dispersion relation becomes unstable in a certain condition for the typical fusion torus device parameters. We also discuss the heat flux density reduction and the heat flux width expansion which may arise from the radial transport by the unstable waves. The details of the unstable mode for the NAGDIS-II linear device parameters are also presented in Sec. 4. Here, the NAGDIS-II contributes to the establishment of the detachment mechanism for future fusion reactors such as ITER and DEMO [26]. The group velocity estimated by the theoretical model is compared with the result of the NAGDIS-II linear device experiment [8]. In Sec. 5 we discuss the dependence of the unstable mode on some physical parameters. Finally, we summarize this work in Sec. 6.

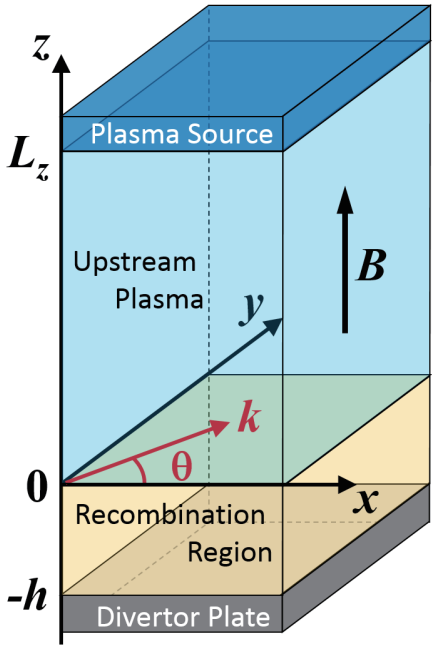

Figure 1. Configuration of the system for the theoretical model. The wave vector $\boldsymbol{k}$ is assumed to be perpendicular to the magnetic field $\boldsymbol{B}$ as $\boldsymbol{k} = (k\cos\theta, k\sin\theta, 0)$.

2. Linear Dispersion Relation

In this study, we have derived the linear dispersion relation from the continuity equations,

$$\frac{\partial n^{\mathrm{P}}}{\partial t} + \nabla_\perp \cdot (n^{\mathrm{P}} \boldsymbol{v}_{s\perp}^{\mathrm{P}}) + \frac{\Gamma_{s\parallel}^{\mathrm{PS}} - \Gamma_{s\parallel}^{\mathrm{B}}}{L_z} = 0 \tag{1}$$

and

$$\frac{\partial n^{\mathrm{R}}}{\partial t} + \nabla_\perp \cdot (n^{\mathrm{R}} \boldsymbol{v}_{s\perp}^{\mathrm{R}}) + \frac{\Gamma_{s\parallel}^{\mathrm{B}} - \Gamma_{s\parallel}^{\mathrm{DP}}}{h} = -\alpha \left[(n^{\mathrm{R}})^2 - (n_0^{\mathrm{R}})^2 \right], \tag{2}$$

and the charge conservation equations,

$$\nabla_\perp \cdot \boldsymbol{j}_\perp^{\mathrm{P}} + \frac{j_\parallel^{\mathrm{PS}} - j_\parallel^{\mathrm{B}}}{L_z} = 0 \tag{3}$$

and

$$\nabla_\perp \cdot \boldsymbol{j}_\perp^{\mathrm{R}} + \frac{j_\parallel^{\mathrm{B}} - j_\parallel^{\mathrm{DP}}}{h} = 0, \tag{4}$$

in the upstream plasma and the recombination region in the simple configuration as shown in Fig. 1. In this configuration, the magnetic field $\boldsymbol{B}$ is parallel to the z axis and the x and y directions correspond to the direction perpendicular to the magnetic flux surface and the toroidal direction in torus devices, respectively. Thus, $\partial B/\partial y = 0$. Furthermore, we assume that the waves propagate in the direction perpendicular to the z axis, that is, the z component of the wave vector is equal to 0, and that the plasma

density n, the electric potential ϕ and the temperature T are uniform in the z direction in each region. Here, $\boldsymbol{v}_{s\perp}$ is the flow velocity perpendicular to the magnetic field, $\Gamma_{s\parallel}$ is the parallel flux, α is the recombination coefficient, $\boldsymbol{j}_\perp$ and $j_\parallel$ are the perpendicular and the parallel currents, the superscripts P, R, B, PS and DP indicate the quantities in the upstream plasma, in the recombination region, at the boundary between those regions ($z = 0$), at the plasma source ($z = L_z$) and at the divertor plate ($z = -h$), respectively, and the subscripts s and 0 represent the particle species and the equilibrium state. The parallel flux at the divertor plate $\Gamma_{s\parallel}^{\mathrm{DP}}$ includes the flux of charged particles provided by the recycling process.

The upstream plasma flow velocity $\boldsymbol{v}_{s\perp}^{\mathrm{P}}$ is composed of the $\boldsymbol{E}\times\boldsymbol{B}$, the polarization and the diamagnetic drifts as

$$\boldsymbol{v}_{s\perp}^{\mathrm{P}} = \frac{(-\nabla_\perp\phi^{\mathrm{P}})\times\boldsymbol{B}}{B^2} - \frac{m_s}{q_s B^2}\left(\frac{\partial}{\partial t} + \boldsymbol{v}_{s\perp}^{\mathrm{P}}\cdot\nabla_\perp\right)(\nabla_\perp\phi^{\mathrm{P}}) + \frac{T_s^{\mathrm{P}}}{q_s B n^{\mathrm{P}}}\left(\frac{\partial n^{\mathrm{P}}}{\partial x}\frac{\boldsymbol{y}}{y} - \frac{\partial n^{\mathrm{P}}}{\partial y}\frac{\boldsymbol{x}}{x}\right), \tag{5}$$

while the recombination region flow velocity $\boldsymbol{v}_{s\perp}^{\mathrm{R}}$ is described by each drift with the Hall mobility μ_{H} and the motion in the direction of the perpendicular electric field with the Pedersen mobility μ_{P} according to the analogy with the ionosphere [21], that is,

$$\boldsymbol{v}_{s\perp}^{\mathrm{R}} = \mu_{\mathrm{H}s}\left[\frac{(-\nabla_\perp\phi^{\mathrm{R}})\times\boldsymbol{B}}{B} - \frac{m_s}{q_s B}\left(\frac{\partial}{\partial t} + \boldsymbol{v}_{s\perp}^{\mathrm{R}}\cdot\nabla_\perp\right)(\nabla_\perp\phi^{\mathrm{R}}) + \frac{T_s^{\mathrm{R}}}{q_s n^{\mathrm{R}}}\left(\frac{\partial n^{\mathrm{R}}}{\partial x}\frac{\boldsymbol{y}}{y} - \frac{\partial n^{\mathrm{R}}}{\partial y}\frac{\boldsymbol{x}}{x}\right)\right] + \mu_{\mathrm{P}s}\frac{q_s}{|q_s|}(-\nabla_\perp\phi^{\mathrm{R}}). \tag{6}$$

Here, m_s and q_s are the mass and the charge of s particle and μ_{H} and μ_{P} are defined by

$$\mu_{\mathrm{H}s} = \frac{|q_s|}{m_s\nu_s}\frac{|\Omega_{cs}|/\nu_s}{1+(\Omega_{cs}/\nu_s)^2} \tag{7}$$

and

$$\mu_{\mathrm{P}s} = \frac{|q_s|}{m_s\nu_s}\frac{1}{1+(\Omega_{cs}/\nu_s)^2}, \tag{8}$$

respectively, in which ν_s is given by

$$\nu_{\mathrm{e}} = \nu_{\mathrm{rec}} + \nu_{\mathrm{en}} + \nu_{\mathrm{ei}} \tag{9}$$

or

$$\nu_{\mathrm{i}} = \nu_{\mathrm{rec}} + \nu_{\mathrm{in}} + \nu_{\mathrm{ie}}. \tag{10}$$

In the discussion in this paper, it is assumed that $\nu_{\mathrm{e}} \sim \nu_{\mathrm{i}}$ and ν_s is replaced with ν_*. Furthermore, the neutral wind term and the collision term are neglected in Eq. (6) because those terms will vanish in the derivation of the dispersion relation under the condition assumed in this paper.

The equilibrium and boundary conditions are given as follows: The equilibrium density and potential are uniform in the toroidal direction as $\partial n_0^{\mathrm{P}}/\partial y = 0$, $\partial n_0^{\mathrm{R}}/\partial y = 0$,

$\partial\phi_0^{\rm P}/\partial y = 0$ and $\partial\phi_0^{\rm R}/\partial y = 0$. The current density at the plasma source ($z = L_z$) is zero and constant in time, that is, $j_\parallel^{\rm PS} = 0$. The equilibrium current density at the boundary is also zero as $j_{\parallel 0}^{\rm B} = 0$. On the other hand, the current density at the divertor plate ($z = -h$) is constant in time and satisfies the relation $j_\parallel^{\rm DP} = h|q_{\rm e}|(-\partial\phi_0^{\rm R}/\partial x)[(\mu_{\rm Pe}+\mu_{\rm Pi})(\partial n_0^{\rm R}/\partial x) - 2n_0^{\rm R}(\mu_{\rm Pe}/B)(\partial B/\partial x)]$ in order to keep the charge conservation. The particle fluxes at $z = L_z$ and $-h$ are also constant in time and equal to the equilibrium flux at the boundary, that is, $\Gamma_{s\parallel}^{\rm PS} = \Gamma_{s\parallel 0}^{\rm B} = \Gamma_{s\parallel}^{\rm DP}$. In this paper, for simplicity, the recycling process included in $\Gamma_{s\parallel}^{\rm DP}$ does not vary even if the plasma density is perturbed. The temperatures in each region are assumed to be uniform and constant in time, i.e., $T_s^{\rm P} = T_{s0}^{\rm P}$, $\partial T_{s0}^{\rm P}/\partial x = \partial T_{s0}^{\rm P}/\partial y = 0$, $T_s^{\rm R} = T_{s0}^{\rm R}$ and $\partial T_{s0}^{\rm R}/\partial x = \partial T_{s0}^{\rm R}/\partial y = 0$.

Linearizing Eqs. (1)–(4), as a result, we obtain the cubic equation regarding the frequency ω as the dispersion relation, that is,

$$\omega^3 + A_2(k,\theta)\,\omega^2 + A_1(k,\theta)\,\omega + A_0(k,\theta) = 0, \tag{11}$$

in which

$$\begin{aligned} A_2 = & -(v_{y0}^{\rm P} + V_{y0}^{\rm P} + V_{y0}^{\rm R})k\sin\theta + {\rm i}\left(\frac{V^{\rm P}}{L_z} + \frac{\partial v_{y0}^{\rm P}}{\partial x}\cos\theta\sin\theta\right) \\ & - A_3\left[\frac{2}{B}\frac{\partial B}{\partial x}v_{\rm Pe}^{\rm R} - \frac{d^{\rm R}}{h} - {\rm i}(V_{\rm P}^{\rm R}\cos\theta + V_{\rm H}^{\rm R}\sin\theta)k\right], \end{aligned} \tag{12}$$

$$\begin{aligned} A_1 = & (v_{y0}^{\rm P}V_{y0}^{\rm R} + V_{y0}^{\rm P}V_{y0}^{\rm R} + v_{y0}^{\rm P}V_{y0}^{\rm P})k^2\sin^2\theta \\ & - \left(\frac{V^{\rm P}}{L_z} + \frac{\partial v_{y0}^{\rm P}}{\partial x}\cos\theta\sin\theta\right)\left(\frac{v^{\rm R}}{2h} + R_0 n_0^{\rm R}\right) \\ & - \frac{V^{\rm P}}{L_z}\frac{\partial v_{y0}^{\rm P}}{\partial x}\cos\theta\sin\theta + \frac{v^{\rm P}V^{\rm R}}{2hL_z} \\ & - {\rm i}\left[\left(V_{y0}^{\rm P}\frac{\partial v_{y0}^{\rm P}}{\partial x}\cos\theta\sin\theta + v_{y0}^{\rm P}\frac{V^{\rm P}}{L_z}\right)k + \frac{\eta d^{\rm P}G}{c_1 Bk}\right. \\ & \quad + \left(\frac{\partial v_{y0}^{\rm P}}{\partial x}\cos\theta\sin\theta + \frac{V^{\rm P}}{L_z}\right)V_{y0}^{\rm R}k \\ & \quad \left. + (v_{y0}^{\rm P} + V_{y0}^{\rm P})\left(\frac{v^{\rm R}}{2h} + R_0 n_0^{\rm R}\right)k\right]\sin\theta \\ & + A_3\left\{\left[\frac{2}{B}\frac{\partial B}{\partial x}v_{\rm Pe}^{\rm R} - \frac{d^{\rm R}}{h} - {\rm i}(V_{\rm P}^{\rm R}\cos\theta + V_{\rm H}^{\rm R}\sin\theta)k\right]\right. \\ & \quad \left[(v_{y0}^{\rm P} + V_{y0}^{\rm P})k\sin\theta - {\rm i}\left(\frac{\partial v_{y0}^{\rm P}}{\partial x}\cos\theta\sin\theta + \frac{V^{\rm P}}{L_z}\right)\right] \\ & \quad \left. - {\rm i}\frac{d^{\rm P}V^{\rm R}}{hL_z}\right\}, \end{aligned} \tag{13}$$

$$A_0 = \frac{\eta d^{\rm R}v^{\rm P}G}{2hc_1Bk}\sin\theta - \frac{v^{\rm P}V^{\rm R}}{2hL_z}\left(v_{y0}^{\rm P}k\sin\theta - {\rm i}\frac{\partial v_{y0}^{\rm P}}{\partial x}\cos\theta\sin\theta\right)$$

$$
\begin{aligned}
&+\mathrm{i}\left[\left(V_{y0}^{\mathrm{P}}\frac{\partial v_{y0}^{\mathrm{P}}}{\partial x}\cos\theta\sin\theta+v_{y0}^{\mathrm{P}}\frac{V^{\mathrm{P}}}{L_z}\right)k+\frac{\eta d^{\mathrm{P}}G}{c_1Bk}\right]\\
&\quad\left[V_{y0}^{\mathrm{R}}k\sin\theta+\mathrm{i}\left(\frac{v^{\mathrm{R}}}{2h}+R_0n_0^{\mathrm{R}}\right)\right]\sin\theta\\
&+A_3\Bigg\{\left[\frac{2}{B}\frac{\partial B}{\partial x}v_{\mathrm{Pe}}^{\mathrm{R}}-\frac{d^{\mathrm{R}}}{h}-\mathrm{i}(V_{\mathrm{P}}^{\mathrm{R}}\cos\theta+V_{\mathrm{H}}^{\mathrm{R}}\sin\theta)k\right]\\
&\quad\left[v_{y0}^{\mathrm{P}}V_{y0}^{\mathrm{P}}k^2\sin^2\theta-\frac{\partial v_{y0}^{\mathrm{P}}}{\partial x}\frac{V^{\mathrm{P}}}{L_z}\cos\theta\sin\theta\right.\\
&\quad\left.-\mathrm{i}\left(\frac{\partial v_{y0}^{\mathrm{P}}}{\partial x}V_{y0}^{\mathrm{P}}\cos\theta\sin\theta+v_{y0}^{\mathrm{P}}\frac{V^{\mathrm{P}}}{L_z}\right)k\sin\theta\right]\\
&\quad-\mathrm{i}\left[\frac{d^{\mathrm{P}}V^{\mathrm{R}}}{hL_z}\left(v_{y0}^{\mathrm{P}}k\sin\theta-\mathrm{i}\frac{\partial v_{y0}^{\mathrm{P}}}{\partial x}\cos\theta\sin\theta\right)\right.\\
&\quad-\frac{\eta d^{\mathrm{P}}G}{c_1B}\sin\theta\\
&\quad\left.\left(\frac{2}{B}\frac{\partial B}{\partial x}\frac{v_{\mathrm{Pe}}^{\mathrm{R}}}{k}-\mathrm{i}(V_{\mathrm{P}}^{\mathrm{R}}\cos\theta+V_{\mathrm{H}}^{\mathrm{R}}\sin\theta)\right)\right]\Bigg\}
\end{aligned}
\tag{14}
$$

and

$$
\begin{aligned}
A_3=\left(\frac{G\ \sin\theta}{2B}\right)\Bigg/\Bigg\{&n_0^{\mathrm{R}}M_{\mathrm{P}}k-\mathrm{i}\left[\frac{n_0^{\mathrm{R}}}{B}\frac{\partial B}{\partial x}\left(\frac{\sin\theta}{B}-2\mu_{\mathrm{Pe}}\cos\theta\right)\right.\\
&\left.+\frac{\partial n_0^{\mathrm{R}}}{\partial x}(M_{\mathrm{P}}\cos\theta-M_{\mathrm{H}}\sin\theta)\right]\Bigg\}.
\end{aligned}
\tag{15}
$$

In the above equations, all variables and coefficients are normalized by $\Omega_{\mathrm{ci}}=q_{\mathrm{i}}B(x=0)/m_{\mathrm{i}}$, $c_{\mathrm{s}}^{\mathrm{P}}=\sqrt{T_{\mathrm{e}}^{\mathrm{P}}/m_{\mathrm{i}}}$, $\rho_{\mathrm{s}}^{\mathrm{P}}=c_{\mathrm{s}}^{\mathrm{P}}/\Omega_{\mathrm{ci}}$, $B(x=0)$ and $n_0^{\mathrm{P}}(x=0)$. Some variables and coefficients which appear in the equations are defined by

$$
v_{y0}^{\mathrm{P}}=\frac{1}{B}\frac{\partial\phi_0^{\mathrm{P}}}{\partial x}+\frac{m_{\mathrm{i}}T_{\mathrm{i}}^{\mathrm{P}}-m_{\mathrm{e}}T_{\mathrm{e}}^{\mathrm{P}}}{|q_{\mathrm{e}}|B(m_{\mathrm{i}}+m_{\mathrm{e}})}\frac{1}{n_0^{\mathrm{P}}}\frac{\partial n_0^{\mathrm{P}}}{\partial x},
\tag{16}
$$

$$
V_{y0}^{\mathrm{P}}=\frac{1}{B}\frac{\partial\phi_0^{\mathrm{P}}}{\partial x}-\frac{m_{\mathrm{i}}T_{\mathrm{e}}^{\mathrm{P}}-m_{\mathrm{e}}T_{\mathrm{i}}^{\mathrm{P}}}{|q_{\mathrm{e}}|B^2(m_{\mathrm{i}}+m_{\mathrm{e}})}\frac{\partial B}{\partial x},
\tag{17}
$$

$$
V_{y0}^{\mathrm{R}}=\frac{1}{2B}\frac{\partial\phi_0^{\mathrm{R}}}{\partial x},
\tag{18}
$$

$$
V^{\mathrm{P}}=2\sqrt{\frac{2}{\pi}}\frac{m_{\mathrm{i}}v_{\mathrm{Te}}^{\mathrm{P}}+m_{\mathrm{e}}v_{\mathrm{Ti}}^{\mathrm{P}}}{m_{\mathrm{i}}+m_{\mathrm{e}}},
\tag{19}
$$

$$
V^{\mathrm{R}}=2\sqrt{\frac{2}{\pi}}\frac{m_{\mathrm{i}}v_{\mathrm{Te}}^{\mathrm{R}}+m_{\mathrm{e}}v_{\mathrm{Ti}}^{\mathrm{R}}}{m_{\mathrm{i}}+m_{\mathrm{e}}},
\tag{20}
$$

$v^{\mathrm{P}}=2\sqrt{2/\pi}(v_{\mathrm{Te}}^{\mathrm{P}}+v_{\mathrm{Ti}}^{\mathrm{P}})$, $v^{\mathrm{R}}=2\sqrt{2/\pi}(v_{\mathrm{Te}}^{\mathrm{R}}+v_{\mathrm{Ti}}^{\mathrm{R}})$, $d^{\mathrm{P}}=2\sqrt{2/\pi}(v_{\mathrm{Ti}}^{\mathrm{P}}-v_{\mathrm{Te}}^{\mathrm{P}})$, $d^{\mathrm{R}}=2\sqrt{2/\pi}(v_{\mathrm{Ti}}^{\mathrm{R}}-v_{\mathrm{Te}}^{\mathrm{R}})$, $v_{\mathrm{Pe}}^{\mathrm{R}}=\mu_{\mathrm{Pe}}(-\partial\phi_0^{\mathrm{R}}/\partial x)$, $V_{\mathrm{P}}^{\mathrm{R}}=M_{\mathrm{P}}(-\partial\phi_0^{\mathrm{R}}/\partial x)$, $V_{\mathrm{H}}^{\mathrm{R}}=M_{\mathrm{H}}(-\partial\phi_0^{\mathrm{R}}/\partial x)$, $M_{\mathrm{P}}=\mu_{\mathrm{Pe}}+\mu_{\mathrm{Pi}}$, $M_{\mathrm{H}}=\mu_{\mathrm{He}}-\mu_{\mathrm{Hi}}$, $\eta=n_0^{\mathrm{P}}/n_0^{\mathrm{R}}$,

$$
c_1=\frac{n_0^{\mathrm{P}}}{n_0^{\mathrm{P}}(x=0)}\frac{L_z}{\rho_{\mathrm{s}}^{\mathrm{P}}}\frac{B^2(x=0)}{B^2}\left(1+\frac{m_{\mathrm{e}}}{m_{\mathrm{i}}}\right),
\tag{21}
$$

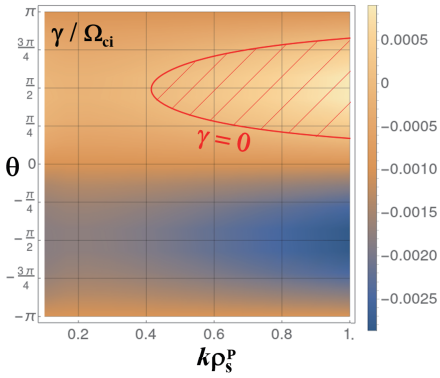

Figure 2. Dependence of the growth rate γ of the unstable mode on the wave number k and the propagation direction θ for the typical fusion device case. The definitions of k and θ are shown in Fig. 1. The hatched area inside the red contour line which represents $\gamma = 0$ designates the unstable region.

$$G = \frac{n_0^{\mathrm{R}}}{B}\frac{\partial B}{\partial x} - \frac{\partial n_0^{\mathrm{R}}}{\partial x}, \tag{22}$$

$R_0 = 2\alpha n_0^{\mathrm{P}}(x=0)/\Omega_{\mathrm{ci}}$, $v_{\mathrm{T}s}^{\mathrm{P}} = \sqrt{T_s^{\mathrm{P}}/m_s}$ and $v_{\mathrm{T}s}^{\mathrm{R}} = \sqrt{T_s^{\mathrm{R}}/m_s}$.

3. Typical Fusion Torus Case

It is found that the one mode of the dispersion relation shown in the previous section has a positive growth rate under a certain condition when the typical parameters for fusion torus devices are assumed. Figure 2 shows the dependence of the growth rate γ of the unstable mode, i.e., the feedback instability mode, on the wave number k and the propagation direction θ. In Fig. 3 we present the dependence of the group velocity $v_{\mathrm{g}} = \partial\omega/\partial k$ of the unstable mode on k and θ. Here, the parameters are set as follows: $B(x=0) = 5$ [T], $\partial B/\partial x = -1$ [T/m], $n_0^{\mathrm{P}}(x=0) = 5\times 10^{19}$ [m^{-3}], $\partial n_0^{\mathrm{P}}/\partial x = -1.67\times 10^{21}$ [m^{-4}], the initial electric fields $-\partial\phi_0^{\mathrm{P}}/\partial x = -\partial\phi_0^{\mathrm{R}}/\partial x = -100$ [V/m], the electron and ion temperatures $T_{\mathrm{e}}^{\mathrm{P}} = T_{\mathrm{i}}^{\mathrm{P}} = 50$ [eV], $T_{\mathrm{e}}^{\mathrm{R}} = T_{\mathrm{i}}^{\mathrm{R}} = 0.3$ [eV], $\nu_*/\Omega_{\mathrm{ci}} = 10$, $R_0 = 10$, $L_z = 10$ [m], $h = 0.3$ [m], the ion-to-electron mass ratio $m_{\mathrm{i}}/m_{\mathrm{e}} = 3.67\times 10^3$ and the ion-to-electron charge ratio $q_{\mathrm{i}}/|q_{\mathrm{e}}| = 1$. In those figures, the hatched area inside the red curve designates the unstable region in which the feedback instability can be induced. Thus, Figs. 2 and 3 indicate that the waves $k\rho_{\mathrm{s}}^{\mathrm{P}} > 0.8$ and $\theta \sim 3\pi/4$ can transport the plasma lump with the speed $\sim 0.002c_{\mathrm{s}}^{\mathrm{P}}$. The simple estimation as mentioned in Fig. 4 shows that the maximum of heat flux density is reduced to $1-(v_{\mathrm{g}x}/c_{\mathrm{s}}^{\mathrm{R}})(\tilde{n}/n_0^{\mathrm{R}})(h/\lambda_{\mathrm{q}}^{\mathrm{B}}) \approx 82$ % of the initial value and that the heat flux width is expanded to $1+(h/\lambda_{\mathrm{q}}^{\mathrm{B}})(v_{\mathrm{g}x}/c_{\mathrm{s}}^{\mathrm{R}}) \approx 280$ % of the initial width if $\tilde{n}/n_0^{\mathrm{R}} \sim 0.1$ and $\lambda_{\mathrm{q}}^{\mathrm{B}} \sim 3$ [mm]. Here, $v_{\mathrm{g}x}$ is the x component of v_{g} and $\tilde{n}$ is the time averaged density of the transported plasma lump.

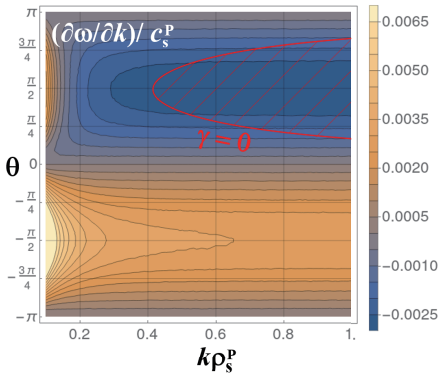

Figure 3. Dependence of the group velocity $\partial\omega/\partial k$ of the unstable mode on the wave number k and the propagation direction θ for the typical fusion device case. The hatched area inside the red contour line which represents $\gamma = 0$ designates the unstable region.

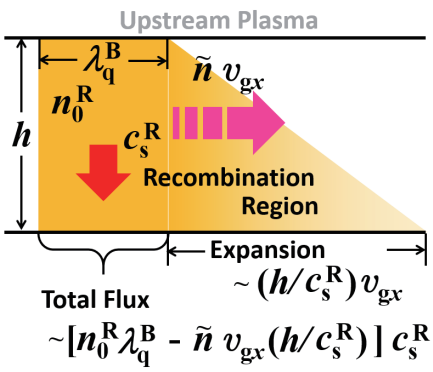

Figure 4. Schematic diagram for the estimations of the heat flux density reduction and the heat flux width expansion. The width of expansion and the total flux for the initial width $\lambda_{\rm q}^{\rm B}$ are estimated as $(h/c_{\rm s}^{\rm R})v_{{\rm g}x}$ and $[n_0^{\rm R}\lambda_{\rm q}^{\rm B} - \tilde{n}v_{{\rm g}x}(h/c_{\rm s}^{\rm R})]c_{\rm s}^{\rm R}$, respectively.

4. NAGDIS-II Linear Device Case

In order to verify the feedback instability model, the spiralling plasma ejection observed around the recombination front under the detached divertor condition in the NAGDIS-II linear device experiment [8] is analysed. Figures 5 and 6 show the dependences of the growth rate γ and the group velocity $v_{\rm g}$ of the feedback instability mode on the wave number k and the propagation direction θ. Here, the parameters are given as follows: $B(x = 0) = 0.075$ [T], $\partial B/\partial x = 0$ [T/m], $n_0^{\rm P}(x = 0) = 1.4 \times 10^{19}$ [m^{-3}], $\partial n_0^{\rm P}/\partial x = -8 \times 10^{20}$ [m^{-4}], $-\partial\phi_0^{\rm P}/\partial x = -\partial\phi_0^{\rm R}/\partial x = -100$ [V/m], $T_{\rm e}^{\rm P} = T_{\rm i}^{\rm P} = 0.7$ [eV], $T_{\rm e}^{\rm R} = T_{\rm i}^{\rm R} = 0.35$ [eV], $\nu_*/\Omega_{\rm ci} = 10$, $R_0 = 10$, $L_z = 1.72$ [m], $h = 0.33$ [m], $m_{\rm i}/m_{\rm e} = 7.33 \times 10^3$ and $q_{\rm i}/|q_{\rm e}| = 1$. Those figures indicate that the waves $k\rho_{\rm s}^{\rm P} < 0.7$ and $\theta \sim \pi/8$ can transport the plasma lump with the speed $\sim 0.2c_{\rm s}^{\rm P}$, that is, with $v_{{\rm g}x} \sim 800$ m/s and $v_{{\rm g}y} \sim 200$ m/s. On the other hand, in the NAGDIS-II experiment,

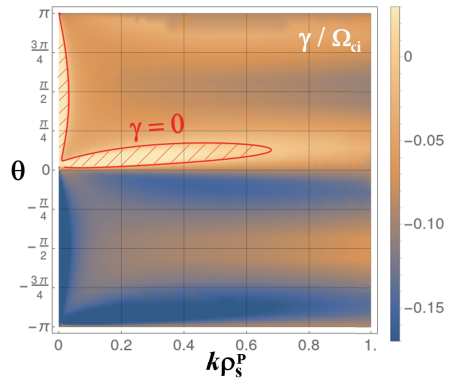

Figure 5. Dependence of the growth rate γ of the unstable mode on the wave number k and the propagation direction θ for the NAGDIS-II linear device case. The hatched area inside the red contour line which represents $\gamma = 0$ designates the unstable region.

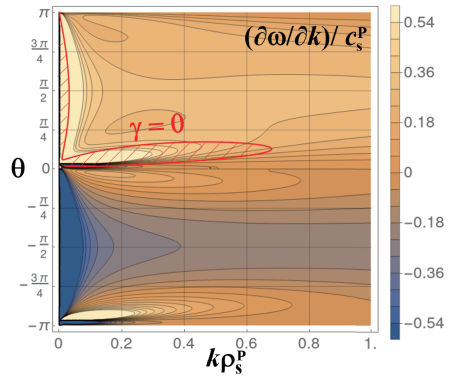

Figure 6. Dependence of the group velocity $\partial\omega/\partial k$ of the unstable mode on the wave number k and the propagation direction θ for the NAGDIS-II linear device case. The hatched area inside the red contour line which represents $\gamma = 0$ designates the unstable region.

the radial speed $v_r \sim 80$ [m/s] at $r \sim 20$ [mm] and azimuthal speed $v_\theta \sim 200$ [m/s] at $r \sim 5$ [mm] are obtained. Here, the plasma configuration in the NAGDIS-II are schematically shown in Fig. 1 in Ref. [8]. Since v_{gx} and v_{gy} correspond to the radial and azimuthal velocities, v_{gy} estimated by the theoretical model is in good agreement with the experiment. On the other hand, v_{gx} estimated by the theoretical model is larger than the radial speed observed in the NAGDIS-II experiment. However, the observed radial speed is detected at the point far from the structure formation area ($r \sim 5$ [mm]). Thus, if v_r increases as r decreases in the NAGDIS-II and the theoretical model is modified to the cylindrical system, the difference between the theoretical estimation and the observation might become small.

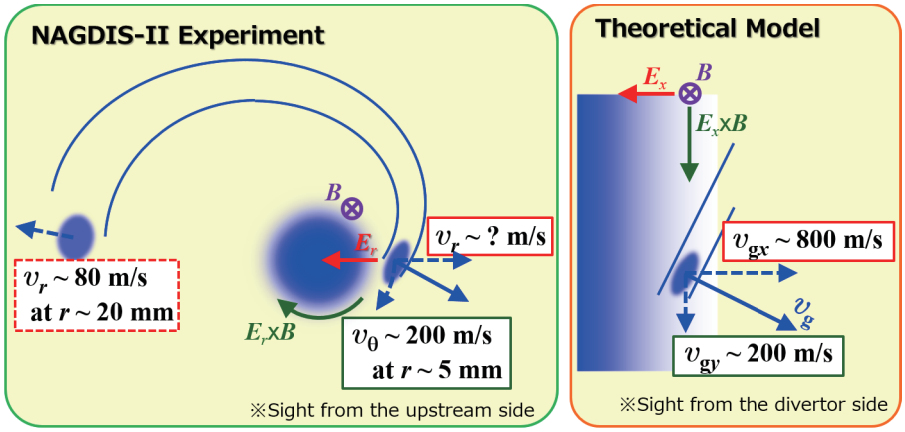

Figure 7. Schematic diagram for the comparison between the NAGDIS-II linear device experiment and the theoretical model.

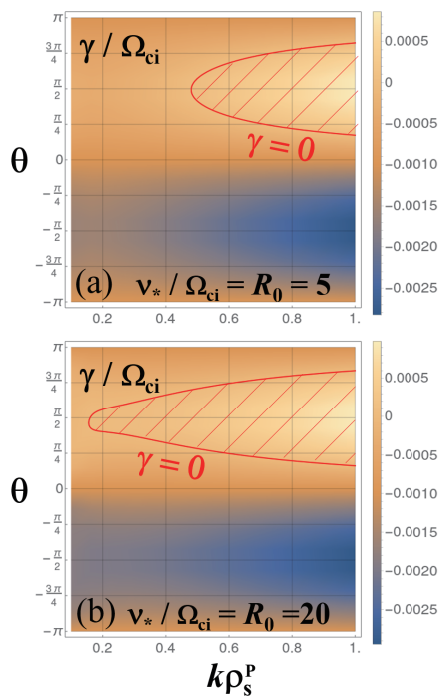

Figure 8. Dependences of the growth rate γ of the unstable mode on the wave number k and the propagation direction θ for $\nu_*/\Omega_{\rm ci} = R_0 = 5$ (a) and 20 (b) for the typical fusion torus case. The hatched area inside the red contour line which represents $\gamma = 0$ designates the unstable region.

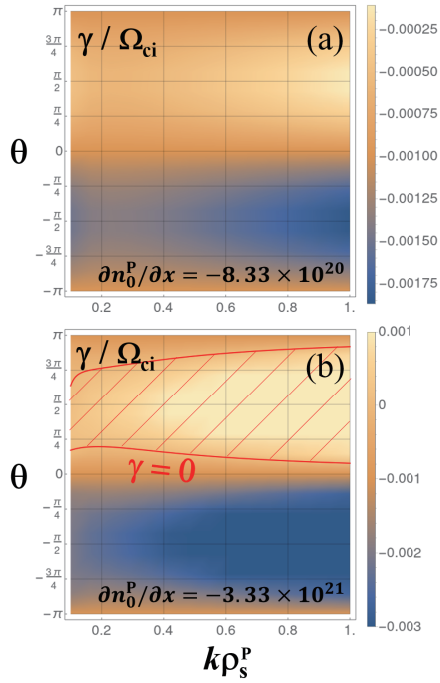

Figure 9. Dependences of the growth rate γ of the unstable mode on the wave number k and the propagation direction θ for $\partial n_0^{\mathrm{P}}/\partial x = -8.33 \times 10^{20}$ [m^{-4}] (a) and -3.33×10^{21} [m^{-4}] (b) for the typical fusion torus case. The hatched area inside the red contour line which represents $\gamma = 0$ designates the unstable region.

5. Dependence on Physical Parameters

In this section we discuss the dependence of the unstable mode on the ratio of the total collision frequency to the ion cyclotron frequency $\nu_*/\Omega_{\mathrm{ci}}$ and the normalized recombination coefficient R_0, and the density gradient in the x direction $\partial n_0^{\mathrm{P}}/\partial x$ for each device case.

5.1. Typical Fusion Torus Case

Figure 8 shows the dependences of the growth rate γ of the unstable mode on the wave number k and the propagation direction θ for $\nu_*/\Omega_{\mathrm{ci}} = R_0 = 5$ and 20. This figure and Fig. 2 indicate that the unstable region in the (k, θ) space is expanded as $\nu_*/\Omega_{\mathrm{ci}}$ and R_0 increase. The reason is thought to be as follows. The increase of $\nu_*/\Omega_{\mathrm{ci}}$ enhances the ion motion in the x direction in the recombination region through the Pedersen mobility. The enhanced ion cross-field motion may contribute to the instability.

Next, the γ distributions of the unstable mode in the (k, θ) space for $\partial n_0^{\mathrm{P}}/\partial x = -8.33 \times 10^{20}$ [m^{-4}] and -3.33×10^{21} [m^{-4}] are represented in Fig. 9. From Figs. 2 and 9, it is found that the unstable region disappears in the lowest density gradient case. On the other hand, the unstable region is extremely expanded with the high density gradient. This fact indicates that the density gradient in the direction perpendicular to

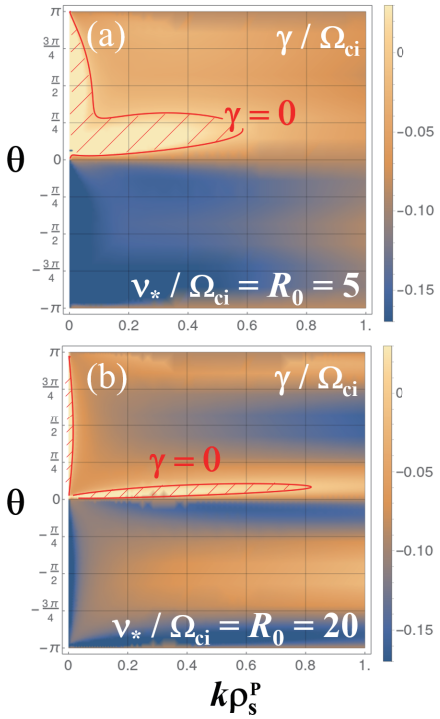

Figure 10. Dependences of the growth rate γ of the unstable mode on the wave number k and the propagation direction θ for $\nu_*/\Omega_{\rm ci} = R_0 = 5$ (a) and 20 (b) for the NAGDIS-II linear device case. The hatched area inside the red contour line which represents $\gamma = 0$ designates the unstable region.

the magnetic flux surface plays an important role in the instability.

5.2. NAGDIS-II Linear Device Case

Figure 10 represents the dependences of the growth rate γ of the unstable mode on the wave number k and the propagation direction θ for $\nu_*/\Omega_{\rm ci} = R_0 = 5$ and 20. This figure and Fig. 5 indicate that the unstable region in the (k, θ) space becomes narrow as $\nu_*/\Omega_{\rm ci}$ and R_0 increase. Although the total collision frequency contributes to the instability in the typical fusion torus case as mentioned in Sec. 5.1, the opposite tendency is shown in the NAGDIS-II linear device case. If $\nu_*/\Omega_{\rm ci}$ and R_0 increase, not only the ion perpendicular motion in the recombination region but also the density reduction by the recombination are enhanced. In the NAGDIS-II linear device case, the density reduction term in Eq. (2) is thought to influence the instability more effectively than the Pedersen term in Eq. (6). This difference between the typical fusion device and the NAGDIS-II is thought to arise from the upstream plasma temperature $T_s^{\rm P}$ and the upstream plasma length L_z. $T_s^{\rm P}$ and L_z for the typical fusion device are larger than those for the NAGDIS-II. Thus, total perturbed perpendicular current in the upstream plasma in the typical fusion device can also become larger than that in the NAGDIS-II. Therefore, in the typical fusion device case, the instability is kept in order to close the

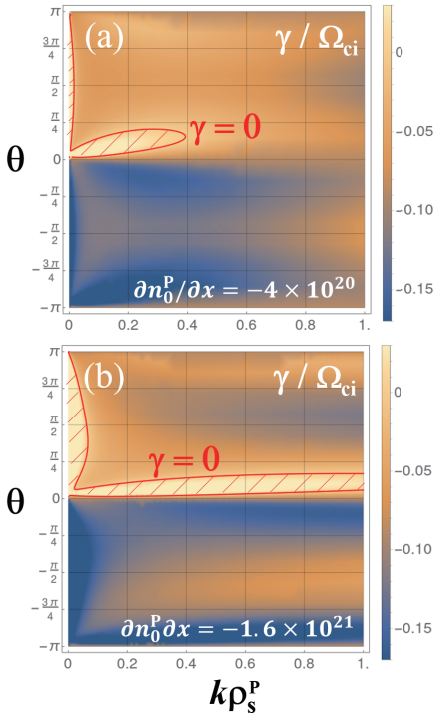

Figure 11. Dependences of the growth rate γ of the unstable mode on the wave number k and the propagation direction θ for $\partial n_0^{\mathrm{P}}/\partial x = -4 \times 10^{20}$ [m^{-4}] (a) and -1.6×10^{21} [m^{-4}] (b) for the NAGDIS-II linear device case. The hatched area inside the red contour line which represents $\gamma = 0$ designates the unstable region.

current circuit even if $\nu_*/\Omega_{\mathrm{ci}}$ and R_0 increases.

On the other hand, the density gradient in the direction perpendicular to the magnetic flux surface also contributes to the instability in the NAGDIS-II linear device case as shown in Fig. 11, which represents the γ distributions of the unstable mode in the (k, θ) space for $\partial n_0^{\mathrm{P}}/\partial x = -4 \times 10^{20}$ [m^{-4}] and -1.6×10^{21} [m^{-4}]. This figure also indicates that the strong gradient induces unstable waves in the shorter wave length region.

6. Summary

The linear dispersion relation for the detached plasma has been derived with the coupling model between the magnetized plasmas characterized by different current mechanisms in the simple configuration. The unstable mode, that is, the feedback instability mode, has been found from the dispersion relation under a certain condition for both the typical fusion device case and the NAGDIS-II linear device case. The heat flux density reduction and the heat flux width expansion have been estimated from the group velocity of the unstable waves for the typical fusion device case. The theoretical result has been also compared with the linear device NAGDIS-II experiment. This comparison indicates that

the feedback instability model might be able to explain the radial transport observed in linear device experiments. Furthermore, the dependence of the feedback instability mode on the total collision frequency and the recombination coefficient and the density gradient has been investigated. Although the dependency on the total collision frequency and the recombination coefficient for the typical fusion torus device case is opposite to that for the NAGDIS-II case, the represented dependencies show the reasonable tendency in each case. In future works, we plan to consider the situations including the temperature fluctuation and the spatial variations in the magnetic field direction. Furthermore, the time variation of the parallel flux provided by the recycling process and the neutral dynamics will be included. The non-linear simulation on the basis of the model will be also performed.

Acknowledgments

This work is performed with the support and under the auspices of the NIFS Collaboration Research programs (NIFS19KNSS119, NIFS21KNSS155, NIFS17KNXN342, NIFS20KNSS134, NIFS19KNXN391, NIFS19KUGM140, NIFS20KNSS136, NIFS19KNTT052, NIFS21KNTT060, NIFS19KNTS058, NIFS21KNTS071 and NIFS19KNTS060), supported by the NINS program of Promoting Research by Networking among Institutions (Grant Number 01421701) and supported by JSPS KAKENHI Grant Numbers JP19K03787, JP16H06139 and JP18KK0410.

References

[1] Krasheninnikov S I and Kukushkin A S 2017 *J. Plasma Phys.* **83** 155830501
[2] Stansfield B L *et al* 1997 *J. Nucl. Mater.* **241–243** 739
[3] Potzel S, Wischmeier M, Bernert M, Dux R, Müller H W, Scarabosio A and the ASDEX Upgrade Team 2013 *J. Nucl. Mater.* **438** S285
[4] Tanaka H, Ohno N, Tsuji Y, Kajita S, Masuzaki S, Kobayashi M, Morisaki T, Tsuchiya H, Komori A and the LHD Experimental Group 2010 *Phys. Plasmas* **17** 102509
[5] Tanaka H, Ohno N, Tsuji Y and Kajita S 2010 *Contrib. Plasma Phys.* **50** 256
[6] Tanaka H, Ohno N, Tsuji Y, Okazaki K and Kajita S 2012 *Contrib. Plasma Phys.* **52** 424
[7] Tanaka H, Takeyama K, Yoshikawa M, Kajita S, Ohno N and Hayashi Y 2018 *Plasma Phys. Control. Fusion* **60** 075013
[8] Tanaka H, Kajita S, Natsume H, Saeki I and Ohno N 2020 *Plasma Phys. Control. Fusion* **62** 075011
[9] Hollmann E M, Pigarov A Y, Seraydarian R, Whyte D G and Krasheninnikov S I 2002 *Phys. Plasmas* **9** 1226
[10] Onda T, Kajita S, Iijima T, Tonegawa A, Ohno N and Tanaka H 2017 *Contrib. Plasma Phys.* **57** 87
[11] Tanaka H *et al* 2018 *Phys. Plasmas* **25** 082505
[12] Tanaka H, Hayashi Y, Kajita S, van der Meiden H J, Yoshikawa M, Vernimmen J W M, Scholten J, Classen I, Morgan T W and Ohno N 2020 *Plasma Phys. Control. Fusion* **62** 115021
[13] Tanaka H, Ohno N, Onda T, Takeyama K, Kajita S, Kuwabara T and Tsuji Y 2016 *Contrib. Plasma Phys.* **56** 723
[14] Takeyama K, Ohno N, Yoshikawa M, Tanaka H and Kajita S 2017 *Plasma Fusion Res.* **12** 1202007

[15] Kajita S, Tanaka H, Ohno N and Onda T 2018 *Plasma Fusion Res.* **13** 1402033
[16] Ohshima H, Kajita S, Tanaka H, Ohno N and van der Meiden H J 2018 *Plasma Fusion Res.* **13** 1201099
[17] Ohno N *et al* 2019 *Nucl. Mater. Energy* **19** 458
[18] Kajita S, Ohshima H, Tanaka H, Seki M, Takano H and Ohno N 2019 *Plasma Sources Sci. Technol.* **28** 105015
[19] Natsume H, Tanaka H, Kajita S, Yoshikawa M, Seki M, Ohshima H and Ohno N 2019 *AIP Advances* **9** 015016
[20] Natsume H, Tanaka H, Kajita S and Ohno N 2020 *Phys. Plasmas* **27** 042301
[21] Hasegawa A and Sato T 1989 *Space Plasma Physics; 1 Stationary Processes* (*Physics and Chemistry in Space* vol 16) (Berlin; Tokyo: Springer-Verlag)
[22] Sato T 1978 *J. Geophys. Res.* **83** 1042
[23] Hasegawa H, Ohno N and Sato T 2010 *J. Geophys. Res.* **115** A08304
[24] Sato T, Hasegawa H and Ohno N 2009 *Comput. Sci. Discovery* **2** 015007
[25] Hasegawa H, Ohno N and Sato T 2011 *Plasma Fusion Res.* **6** 2401128
[26] Ohno N *et al* 2001 *Nucl. Fusion* **41** 1055